Extracting phreatic evaporation from remotely sensed maps of evapotranspiration

P. Brunner,[1,2] H. T. Li,[1] W. Kinzelbach,[1] W. P. Li,[3] and X. G. Dong[4]

Received 25 March 2007; revised 23 April 2008; accepted 20 May 2008; published 23 August 2008.

[1] One of the most important parameters related to soil salinization is the direct evaporation from the groundwater (phreatic evaporation). If the groundwater table is sufficiently close to the surface, groundwater will evaporate through capillary rise. In recent years, several methods have been suggested to map evapotranspiration (ET) on the basis of remote sensing images. These maps represent the sum of both transpiration of vegetation and evaporation from the bare soil. However, identifying the amount of phreatic evaporation is important as it is the dominant flux in the salt balance of the soil. The interpretation of stable isotope profiles at nonirrigated areas in the unsaturated zone allows one to quantify phreatic evaporation independently of the transpiration of the vegetation. Such measurements were carried out at different locations with a different depth to groundwater. The benefit is twofold. (1) A relation between phreatic evaporation rates and the depth to groundwater can be established. (2) By subtracting the measured values of phreatic evaporation from remotely sensed values of ET, vadose ET consisting of transpiration and excess irrigation water in the unsaturated zone can be estimated at the sampling locations. A correlation between the normalized differential vegetation index and the calculated vadose ET rates could be established ($R^2 = 0.89$). With this correlation the contribution of phreatic evaporation can be estimated. This approach has been tested for the Yanqi basin located in western China. Finally, the distribution of phreatic evaporation was compared to a soil salinity map of the project area on a qualitative basis.

Citation: Brunner, P., H. T. Li, W. Kinzelbach, W. P. Li, and X. G. Dong (2008), Extracting phreatic evaporation from remotely sensed maps of evapotranspiration, *Water Resour. Res.*, *44*, W08428, doi:10.1029/2007WR006063.

1. Introduction

[2] In semiarid and arid regions, the salinization of soil is often a consequence of a high groundwater table. Besides deforestation, irrigation is the most common cause of a high groundwater table. In areas irrigated without adequate drainage, the excess irrigation water raises the groundwater table. Salt that has been stored in the unsaturated zone for decades is dissolved in the rising groundwater. If a critical depth to groundwater is reached, groundwater can directly evaporate through capillary rise (phreatic evaporation) and the dissolved salt accumulates in the root zone. Comprehensive overviews covering most of the causes, consequences and possibilities to tackle the problem of salinization can be found in work by *Hillel* [2000], *Jakeman et al.* [1995], and *Richards* [1954], to mention but a few examples.

[3] The spatial distribution of phreatic evaporation is often heterogeneous. Nevertheless, the existing approaches to assess phreatic evaporation yield only point data. Several approaches to estimate groundwater evaporation have been published. *Tyler et al.* [1997] estimated the evaporation rate at Owens Lake in eastern California by combining interpreted chloride profiles with eddy correlation methods. *Ullman* [1995] estimated evaporation rates from Lake Frome, South Australia by interpretation of Cl, Br profiles using an advection/diffusion model. *Barnes and Allison* [1988] have estimated the evaporation rate on the basis of stable isotope profiles. They point out that a principal advantage of using stable isotopes in the determination of water movement in soil is the limited variability of the effective diffusivity with varying water content. Another advantage pointed out by *Barnes and Allison* [1988] is that temperature effects appear to have little effect on stable isotope profiles.

[4] Even though several methods have been presented to estimate phreatic evaporation, the combination of such estimates with remote sensing data is still missing. In this paper, a method is suggested to efficiently map the spatial distribution of phreatic evaporation on a regional scale. The method is tested in the Yanqi basin located in western China. The distribution obtained was used to assess the spatial distribution of the risk of soil salinization. In a final step, the distribution of phreatic evaporation is compared to a soil salinity map.

2. Overview

[5] The method is based on the combination of remote sensing images and measurements of phreatic evaporation on the ground. The spatial distribution of evapotranspiration

[1]Institute of Environmental Engineering, ETH Zurich, Zurich, Switzerland.
[2]Now at School of Chemistry, Physics and Earth Sciences, Flinders University, Adelaide, South Australia, Australia.
[3]China Institute of Geo-Environmental Monitoring, Beijing, China.
[4]Xinjiang Agricultural University, Urumqi, China.

0043-1397/08/2007WR006063

is calculated on the basis of NOAA-AVHRR images. Evapotranspiration (ET) is the sum of the transpiration (T) from vegetation and evaporation. Evaporation includes both phreatic evaporation (E_P) from the groundwater and water stored above the zero-flux plane (E_{Soil}):

$$ET = T + E_{\mathrm{Soil}} + E_P \quad (1)$$

For the salt balance, mainly the phreatic evaporation is of interest. The goal is therefore to separate phreatic evaporation from both the soil evaporation and transpiration related to irrigation. If the amount of rainfall is negligible in an irrigated area, E_{Soil} is irrigation water that has not been consumed by plants. Both transpiration T and E_{Soil} are therefore dependent on the amount of irrigation water applied. The dependency of T and E_{Soil} on the amount of irrigation water applied suggests to combine these two parameters. We combine irrigation related evaporation and transpiration into one parameter, $ET_{\mathrm{V,NOAA}}$ (V stands for vadose ET).

[6] If vegetation growth is highly dependent on irrigation, the normalized differential vegetation index (NDVI) reflects the intensity of irrigation. Such a dependency applies to average data over an irrigation cycle. Consequently, the subsequent discussion focuses on annual values rather than on instantaneous values of ET and NDVI. In areas where no irrigation takes place, the NDVI is expected to be far below the NDVI of irrigated areas. If the irrigation efficiency as well as the dependency of the NDVI on the amount of irrigation water applied is uniform over a given area, we can write

$$ET_{\mathrm{V,NOAA}} = T + E_{\mathrm{Soil}} = f(NDVI) \quad (2)$$

[7] In contrast to $\mathrm{ET_{V,NOAA}}$, phreatic evaporation mainly depends on the depth to groundwater. In order to separate phreatic evaporation from the irrigation related transpiration and evaporation, phreatic evaporation was calculated at a number of nonirrigated observation points on the basis of δ^{18}O profiles in the unsaturated zone. This approach takes advantage of the fact that the isotopically heavier composites of water (such as H_2 δ^{18}O) are enriched during evaporation. In the following we define phreatic evaporation that was estimated on the basis of stable isotopes as $\mathrm{E_{P,ISO}}$.

[8] The combination of annual ET estimates and the isotope data makes it possible to separate evapotranspiration into phreatic evaporation and irrigation related soil evaporation and transpiration. Figure 1 gives an overview of the method. In a first step, ET and the NDVI are mapped on the basis of NOAA-AVHRR images for several days of the year. An annual value of ET (ET_{NOAA}) is calculated by extrapolating the available, daily data. In analogy to equation (1), ET_{NOAA} consists of transpiration from vegetation T, soil evaporation E_{Soil} and phreatic evaporation $E_{\mathrm{P,NOAA}}$. $E_{\mathrm{P,NOAA}}$ represents the contribution of phreatic evaporation to ET_{NOAA}:

$$ET_{\mathrm{NOAA}} = E_{\mathrm{Soil}} + T + E_{\mathrm{P,NOAA}} = ET_{\mathrm{V,NOAA}} + E_{\mathrm{P,NOAA}} \quad (3)$$

[9] In a second step, the phreatic evaporation rates $E_{\mathrm{P,ISO}}$ are calculated for the locations where isotope data from the soil profiles are available. Under the assumption that $E_{\mathrm{P,ISO}}$ equals $E_{\mathrm{P,NOAA}}$, $ET_{\mathrm{V,NOAA}}$ can be estimated at the sampling locations:

$$ET_{\mathrm{V,NOAA}} \approx ET_{\mathrm{NOAA}} - E_{\mathrm{P,ISO}} = f(NDVI) \quad (4)$$

The assumption implies that a point value of phreatic evaporation rate $E_{\mathrm{P,ISO}}$ is representing the phreatic evaporation rate over the entire pixel. The implications of this assumption are discussed in the last section of this contribution.

[10] If a correlation between $ET_{\mathrm{V,NOAA}}$ and the NDVI can be found, the pointwise calculated $ET_{\mathrm{V,NOAA}}$ rates can be regionalized and a continuous map of vadose ET can be calculated. Phreatic evaporation rates of 7 stations were calculated and the corresponding $ET_{\mathrm{V,NOAA}}$ rates were plotted as a function of the NDVI. A very good correlation ($R^2 = 0.89$) between the $ET_{\mathrm{V,NOAA}}$ and the NDVI could be established, justifying the string of assumptions made within this approach.

[11] In the following, the project area is described. The calculation of evapotranspiration based on remote sensing images, the determination of phreatic evaporation as well as the combination of the two quantities and the assumptions made are discussed in more detail.

3. Project Area

[12] The project area is the Yanqi basin, located in the Chinese province of Xinjiang (see Figure 2). The annual amount of precipitation of around 50 mm a^{-1} is negligible compared to the potential evapotranspiration of 1400 mm a^{-1}. Nevertheless, the Yanqi basin has been one of the most productive agricultural areas in western China ever since irrigation was introduced in the second half of the 20th century. Irrigated water is drawn from the rivers flowing through the basin. At present, the irrigated area covers about 1.2×10^5 ha. Even within the intensively irrigated areas of the basin, the fields are small (<1 km^2) and the density of vegetation is low. The dominant crops grown are wheat and corn. Additionally, cotton, grapes and chilli are planted in the area. The irrigation area is split up into four irrigation zones with a homogeneous distribution of crops within. The dominant crops are planted only once a year. Irrigation starts normally at the beginning of April and the seedlings are brought out shortly afterward. The crops are harvested around October. If it weren't for irrigation, vegetation would grow only along the rivers and the lake shore. The intensive irrigation agriculture has led to several environmental problems in the Yanqi basin, especially soil salinization. According to *Dong et al.* [2001], 60% of the irrigated area exhibited a depth to groundwater smaller than 2 m in the year 2000.

[13] The Yanqi basin features large groundwater resources recharged by the rivers flowing through it. The stratigraphy along the mountain range is mainly composed of moraine and glaciofluvial sediments, such as loam and gravel [*Lin et al.*, 2002]. These sediments (also called Gobi formation) feature a high hydraulic permeability. Between the surrounding mountains and the central area of the Yanqi basin, these sediments form a weakly heterogeneous aquifer down to the bedrock. No agriculture is carried out in these regions and the depth to groundwater is large (>10 m). The central area of the Yanqi basin is the only area where soil

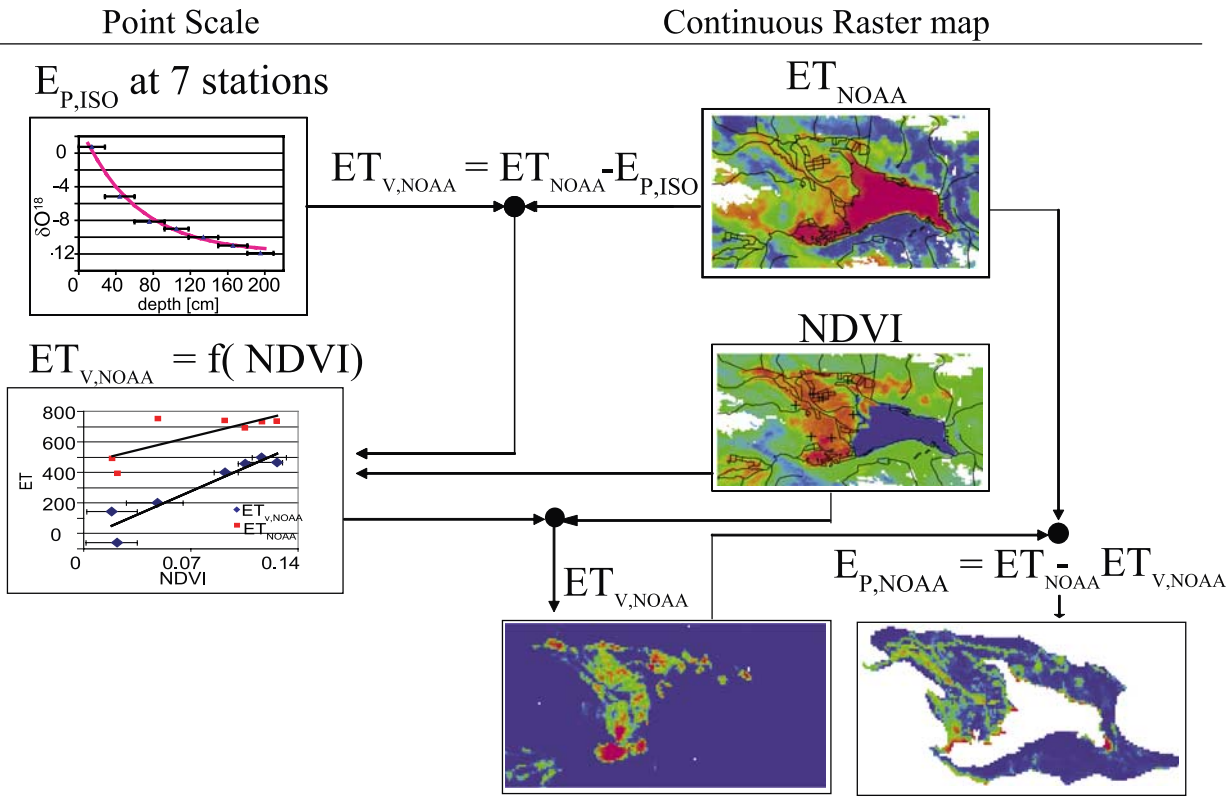

Figure 1. Schematic overview of calculation of phreatic evaporation. $E_{P,ISO}$ is the phreatic evaporation rate calculated on the basis of stable isotopes. The values obtained by using this method represent a long-term average rather than an instantaneous value. ET_{NOAA} is defined as the total annual evapotranspiration rate based on the NOAA-AVHRR images. This annual value is calculated by extrapolating between several daily estimates of ET. $ET_{V,NOAA}$ is the vadose ET rate obtained by the combination of ET_{NOAA} and $E_{P,ISO}$. The NDVI is the normalized differential vegetation index. The NDVI represents an annual average. $E_{P,NOAA}$ is the phreatic evaporation rate, calculated by the combination of $ET_{V,NOAA}$, the NDVI, and ET_{NOAA}.

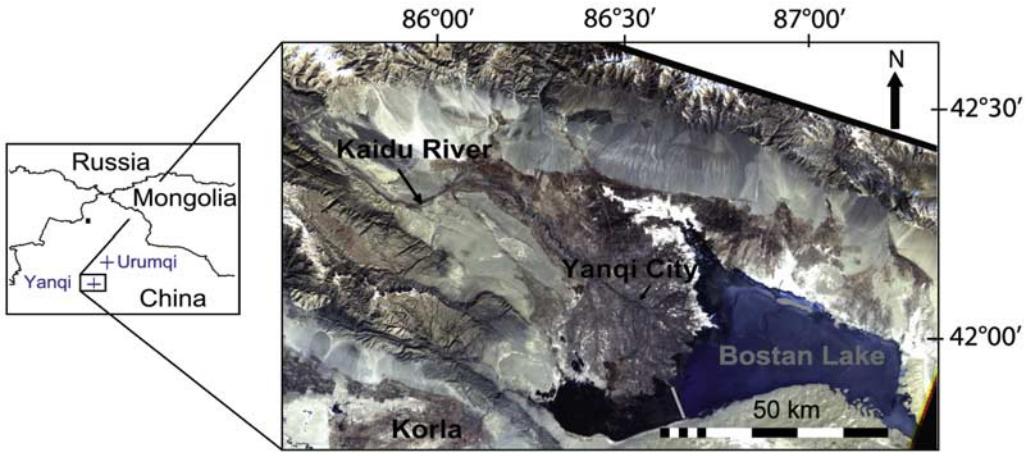

Figure 2. Location of the Yanqi basin. The area west of Bostan Lake is called the ''little lake,'' a swamp with dense reed. The two lakes are separated by a dam, indicated by the solid gray line. The irrigated zones can easily be distinguished from the nonirrigated areas because there is no natural growth of vegetation except along the rivers and around the lake.

could develop and agriculture is possible. The large amount of salt deposited over time in the unsaturated zone is the main source leading to the secondary soil salinization. Typically, the depth to groundwater in the central regions is small and the risk of soil salinization is high.

4. Methods

4.1. Remote Sensing

4.1.1. Remote Sensing of ET

[14] Various methods have been suggested to estimate evapotranspiration. The classical methods at field scale include evaporation pans, eddy correlation systems, bowen ratios or soil water balances. A popular method often used by irrigators to estimate crop ET on the basis of standard meteorological parameters is described by *Allen et al.* [1998]. These methods yield point values. However, for applications such as regional hydrologic modeling, point measurements of ET are insufficient.

[15] Several methods have been suggested to estimate evapotranspiration from remote sensing data [*Carlson and Buffum*, 1989; *Carlson et al.*, 1995; *French et al.*, 2003; *Jiang and Islam*, 1999, 2001; *Kustas et al.*, 1994; *Kustas and Norman*, 1996; *Laymon et al.*, 1998; *Nishida et al.*, 2003; *Thunnissen and Nieuwenhuis*, 1990; *Bastiaanssen et al.*, 1998a, 1998b; *Roerink et al.*, 2000; *Su*, 2002; *Menenti and Choudhury*, 1993]. A good overview of different methods and a sensitivity analysis for various parameters is found in work by *Kempf and Tyler* [2006]. *Nagler et al.* [2005] related evapotranspiration along the Rio Grande to remotely sensed indices. A classification of different methods is given by *Courault et al.* [2005]. The key to estimate the latent heat flux on the basis of remote sensing data is the calculation of a surface energy balance. For instantaneous conditions the surface energy balance is given by

$$R_n = \lambda E + H + G_0 \tag{5}$$

R_n is defined as the net energy. This energy is available for the latent heat flux λE, the sensible heat flux H and the soil heat flux G_0. These quantities refer to the specific moment in time when the image is taken. The units for all fluxes are W m^{-2}.

[16] For many applications, an estimate of a daily ET rate is of greater interest than an instantaneous rate. In principle, a daily rate can be calculated by assuming a sinusoidal course of ET during the day. Other conversions are based on the properties of the evaporative fraction. The evaporative fraction ε is defined as

$$\varepsilon = \frac{\lambda E}{\lambda E + H} = \frac{\lambda E}{R_n - G_0} \approx \frac{\lambda E}{R_n} \tag{6}$$

Shuttleworth et al. [1989] and *Gurney and Hsu* [1990] reported that the evaporative fraction remains constant over the day. *Sugita and Brutsaert* [1991] and *Brutsaert and Sugita* [1992] tested and confirmed this relationship. A discussion and interpretation of these studies is given by *Crago* [1996]. He concluded that the variability of the evaporative fraction is related to the cloudiness and the advection of moisture and temperature during the day, but in many cases is indeed constant. A study carried out by *Zhang and Lemeur* [1995] compared ET estimates based on a sinusoidal course with daily estimates based on the assumption of a constant evaporative fraction. In agreement with the findings of *Crago* [1996] they achieved a good agreement for the two methods for cloud-free days. A constant evaporative fraction allows one to calculate a daily ET rate on the basis of a remote sensing image of a specific moment in time. In our notation, the daily ET (ET_{NOAA}) is written as the product of the average daily net radiation $\overline{R_n}^{\mathrm{day}}$ and the evaporative fraction ε:

$$ET_{\mathrm{NOAA}}(x,y,t) = \varepsilon(x,y,t) \cdot \overline{R_n}^{\mathrm{day}}(x,y,t) \tag{7}$$

The daily net radiation can be calculated from satellite imagery and astronomical data by using standard algorithms as described, e.g., by *Parodi* [2002].

[17] In this study, the simplified surface energy balance index (S-SEBI) suggested by *Roerink et al.* [2000] was used to estimate the evaporative fraction on the basis of NOAA-AVHRR images. Under the assumption of a constant daily evaporative fraction, daily values of ET were calculated. S-SEBI estimates atmospheric turbulent fluxes and the evaporative fraction on the basis of satellite data. The big advantage of S-SEBI compared to other methods is that no additional meteorological data are required. Only a limited amount of meteorological data is available for the project region, making S-SEBI especially useful for this study. Another advantage is that no fixed temperature for wet and dry conditions has to be determined.

[18] According to *Roerink et al.* [2000], the evaporative fraction for each pixel of the satellite image can be extracted by plotting all pixels of the image in a coordinate system of the surface temperature T_{surf} versus the ground albedo r_{surf}. Well-watered dense crops tend to have cool temperatures and low albedo while dry soil often features a high temperature and a high albedo.

[19] A feature plot of r_{surf} versus T_{surf} is shown in Figure 3. The method assumes that points along the line AB are completely wet, in contrast to points along CB. These pixels are completely dry and the latent heat is zero. In Figure 3 the example of a pixel at P is shown. According to Roerink, the evaporative fraction is given by

$$\varepsilon = \frac{\overline{PC}}{\overline{AC}} \tag{8}$$

$\overline{PC}$ is the temperature difference between point P and C and $\overline{AC}$ is the temperature difference between point A and C.

[20] The precondition to use this method is that both dry and wet pixels are contained in the image of consideration. Wet pixels are found in Bostan Lake and completely dry areas are also present in the nonirrigated areas.

4.1.2. Processing NOAA-AVHRR Images for the Yanqi Basin

[21] All calculations with remote sensing data are based on NOAA-AVHRR images (NOAA 14). NOAA-AVHRR images have a 1 km by 1 km resolution at Nadir and feature five spectral channels. The spatial resolution of the images varies with the viewing angle. The images were resampled to ensure an identical spatial resolution for all processed images. All images were absolutely georeferenced with respect to ground points of a known geographical location.

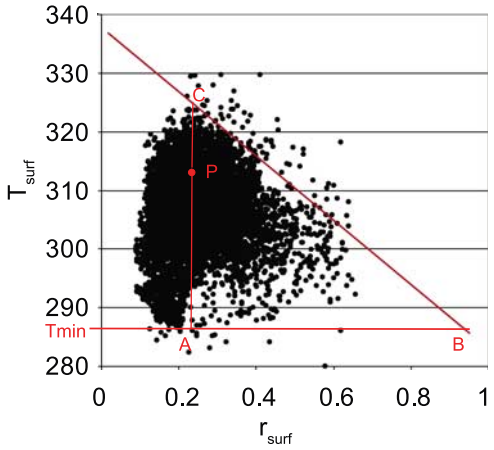

Figure 3. Feature space plot between albedo r_{surf} (Kelvin) and temperature T_{surf} (Kelvin) for an image over the project area (image date 27 April 2000).

The accuracy of the georeference is of the magnitude of one pixel. The calculation of parameters such as surface temperature, planetary broadband albedo or the daily net radiation was carried out according to the methods outlined by *Parodi* [2002] (http://www.itc.nl/research/products/_docs/AHAS_algorithms_and_theory_v3.pdf). In a first step the planetary broadband albedo r_p is calculated by using a linear model described by *Valiente et al.* [1995]:

$$r_p = c1 + c2*CH1 + c3*CH2 \tag{9}$$

CH1 and CH2 are the NOAA-AVHRR image bands. According to Valiente, the weighting factors for NOAA-AVHRR images are: $c1 = 0.035$, $c2 = 0.545$ and $c3 = 0.32$. The planetary broadband albedo was converted to a broadband surface albedo r_0 according to a method suggested by *Chen and Ohring* [1984]:

$$r_0 = \frac{r_p - c4}{c5} \tag{10}$$

Here $c4$ is the offset in the relationship between broadband planetary albedo and broadband surface albedo. As an approximation, the lowest value of the planetary albedo can be applied. c5 is the two way transmittance of the broadband shortwave radiation (0.5).

[22] The surface temperature was calculated with the split window technique. The parameters used were suggested by *Coll and Caselles* [1997]. S-SEBI relates different surface temperatures to changes in the energy balance (including the latent heat flux). Changes of temperature due to differences in the elevation have to be taken into account. Low temperatures in high elevations are not only related to the cooling effect of water, the temperature difference is related to the increased terrain elevation. In this study, the correction was based on the Shuttle Radar Topography Mission (SRTM) digital elevation model. An assessment of the SRTM data is given by *Rodriguez et al.* [2005]. An average laps rate of 0.0065°C m^{-1} was used [*Wallace and Hobbs*, 2006]. The SRTM model has a spatial resolution of 90 m by 90 m. The DEM was resampled to the same resolution as the NOAA-AVHRR images.

[23] In total, 14 images were processed. Surface temperature and albedo were calculated as described above. The slope of the line CB in the feature plots was determined graphically. All images featured a clear decrease of pixels along the upper line of the triangle. Its exact position was determined with the constraint that at least 99% of the pixels had to be included within the triangle. In most images, the minimum temperature is found in Bostan Lake.

4.1.3. Estimation of the Annual ET Over the Project Area

[24] The daily ET rates (average over the entire image) obtained on the basis of remote sensing data were compared to a potential ET calculated on the basis of the Penman-Monteith equation. The required input data for the Penman-Monteith equation were measured in Korla, the only available meteorological station close to the project area. The average ET over the images processed was compared to the potential evapotranspiration calculated for Korla. The comparison is plotted in Figure 4. The linear regression between the two quantities is given by

$$ET_{pot} = 2.39*ET_{NOAA} + 0.5135 \tag{11}$$

The correlation coefficient R^2 between the two quantities is 0.95. The high correlation coefficient between the two quantities suggests that the average values for actual ET for dates where no NOAA-AVHRR images are available can be approximated on the basis of potential ET.

[25] In order to assess the annual variation of the patterns of ET, a principal component analysis of the processed maps was carried out. The first component is 0.92. This analysis suggests that the patterns of ET are constant in time. Considering the hydrological framework of the Yanqi basin, this is expected. The patterns of ET are linked to features in the project area that do not move. The most obvious example is Bostan Lake. Irrigated areas are another large evaporative feature. Their position remains also constant as irrigation in the Yanqi basin is applied in a uniform

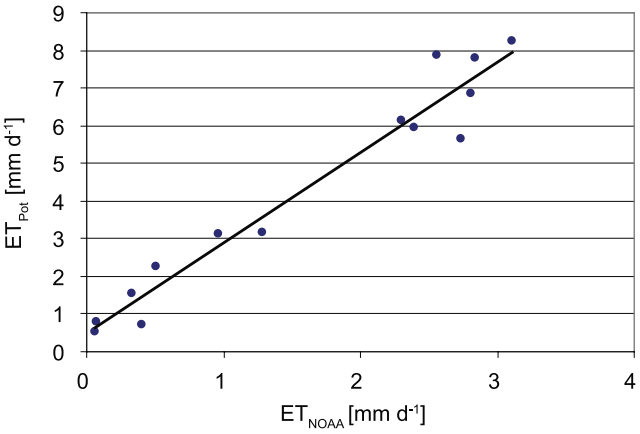

Figure 4. Comparison between the average ET estimates based on remote sensing (ET_{NOAA}) and the potential ET rates (ET_{Pot}) for Korla for the days NOAA-AVHRR images were available. The total annual ET calculated by using the Penman-Monteith equation is 1.4 m a^{-1}.

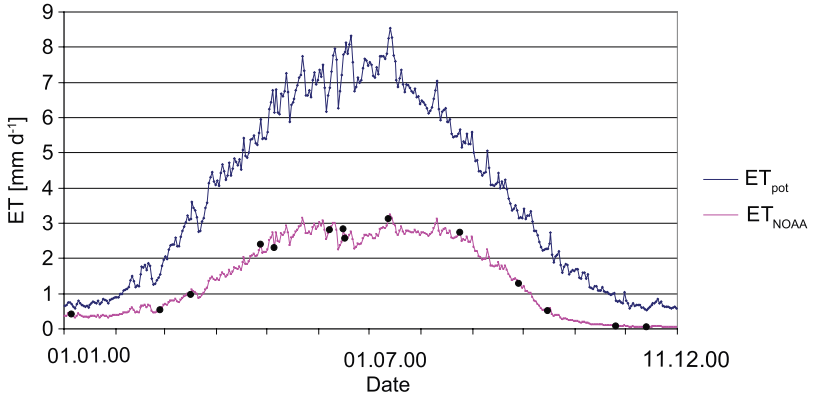

Figure 5. Potential ET calculated for Korla, year 2000. The actual ET (ET_{NOAA}) was determined for 14 days on the basis of the NOAA-AVHRR images. These days are indicated with black dots. Values for dates where no images were available were calculated on the assumption that the ratio between ET_{POT} and ET_{NOAA} is linear.

way. The nonirrigated areas, on the other hand, have a small ET rate throughout the year.

[26] The constant evaporation patterns and the high correlation between ET_{NOAA} and the potential evaporation rate (equation (11)) allow to interpolate the images in time. *Allen et al.* [2007] suggested a seasonal extrapolation method to interpolate between images. In this approach, we approximated the average ET rate for days between the available remote sensing images by using a linear interpolation of the ratio between ET_{NOAA} and the potential evaporation rate of the available images. This allows one to provide the target daily scene-average ET. The course of potential ET for the year 2000, as well as the actual ET based on the linear interpolation of the ratio ET_{NOAA} to the potential evaporation are presented in Figure 5. The spatial distribution of these estimates of the daily, average ET was assumed to be identical to the closest available, processed image. The total annual ET for the year 2000 is presented in Figure 6.

4.1.4. NDVI

[27] The NDVI is a measure of the vigor of vegetation. The NDVI is calculated from the atmospherically corrected NOAA channels 1 and 2:

$$NDVI = \frac{CH2 - CH1}{CH2 + CH1} \tag{12}$$

[28] Calculation of NDVI for a given pixel results in a number that ranges from −1 to +1. If a pixel is covered with dense vegetation, the NDVI gets close to 1. No vegetation results in a NDVI of 0, negative values indicate the presence of water.

[29] In the Yanqi basin, the highest monthly NDVI values are found in the reed zones of the little lake (0.6). In the irrigated areas, the highest (monthly) NDVI values observed are around 0.32. This is a relatively low value but it is expected as fields are much smaller than 1 km^2: Even in the intensively irrigated areas of the Yanqi basin fields do not cover an area of 1 km by 1 km. The cropping cycle is reflected by the change of NDVI through the year. After the crops are planted in April, the irrigation areas can be clearly distinguished from the nonirrigated areas until the crops are harvested in October. In wintertime temperatures do not allow the growth of vegetation and consequently the NDVI is 0.

[30] The same images used to calculate ET were used for the NDVI. In contrast to ET, the NDVI does not vary on a daily basis. For the comparison with $ET_{V,NOAA}$, the average of all available images was calculated. This map is presented in Figure 7. The principal component analysis confirmed also for the NDVI that the pattern over the year is very stable.

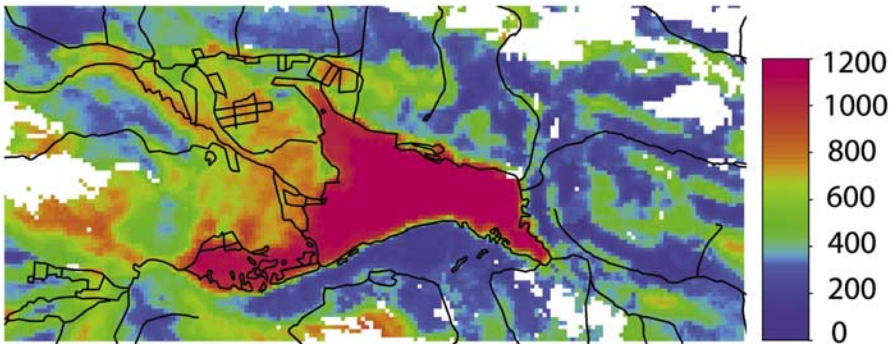

Figure 6. Evapotranspiration ET_{NOAA} (mm a^{-1}) over the project area for the year 2000. The white pixels were covered with cloud or were the shadows/edges of the clouds in at least one image. These areas have been masked out and are not calculated.

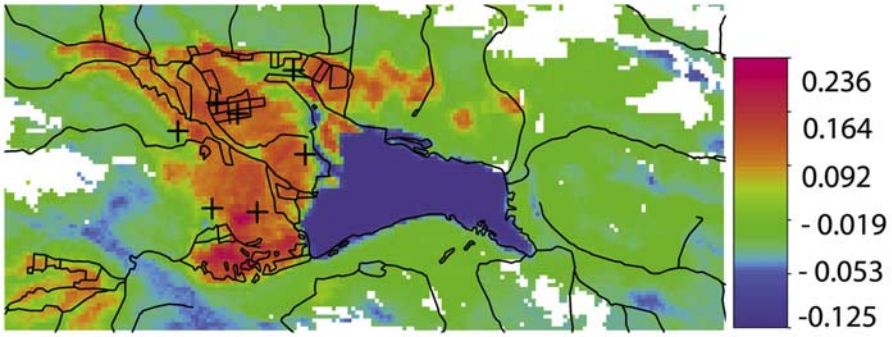

Figure 7. Average of the NDVI (dimensionless) of the processed images (year 2000) over the project area. The white pixels were covered with cloud in at least one image and therefore cannot be calculated. The lower limit of the color scale has been cut at −0.125. The crosses indicate the (nonirrigated) soil sampling stations where phreatic evaporation was determined.

4.2. Calculating Phreatic Evaporation on the Basis of Isotope Profiles

[31] Evaporation rates independent of vegetation can be calculated by using the distribution of stable isotopes in a nonirrigated soil column. If this distribution is measured at different sites with a different depth to groundwater, a relation between the evaporation rate and depth to groundwater can be established.

4.2.1. Theoretical Background

[32] An analytical model describing the movement of isotopic components in water evaporating from a free water body into the atmosphere was developed by *Craig and Gordon* [1965]. *Zimmermann et al.* [1967] demonstrated that the enrichment of deuterium in the soil water of a saturated soil column decreases with depth. The profile of deuterium could be approximated by an exponential function with a decay length approximately proportional to the evaporation rate. These findings were explained as the result of a superposition between diffusive and convective fluxes through the soil column. The isotopic profile in a saturated soil can be described by

$$R(z) = R_\infty + (R_{\text{eff}} - R_\infty) \cdot e^{-\frac{z}{z_l}} \tag{13}$$

$R(z)$ is the isotopic signature as a function of the depth z, R_∞ is the isotope ratio of the water entering the column from below. z_l is defined as

$$z_l = \frac{\theta \cdot f \cdot D}{E_{\text{P,ISO}}} \tag{14}$$

where $E_{\text{P,ISO}}$ is the phreatic evaporation rate [m s^{-1}], θ the volumetric water content, f the tortuosity factor of the soil and D the self-diffusion coefficient for liquid water. D is 1.77×10^{-9} m^2 s^{-1} at 15°C [*Mills*, 1973] and the tortuosity factor for sandy soils is around 0.66. *Barnes and Allison* [1988] extended this concept to unsaturated soils. The isotopic profile in an unsaturated soil column can be expressed as a function of depth in analogy to equation (13):

$$R(z) = R_\infty + (R_{\text{eff}} - R_\infty) \cdot e^{-\frac{z - z_{\text{ef}}}{z_v + z_l}} \tag{15}$$

where z_{ef} is the depth of the evaporating front; z_v is defined as

$$z_v = \frac{D_v \cdot N^{\text{sat}}}{\rho \cdot E_{\text{P,ISO}}} = \frac{(n - \theta) \cdot f \cdot D_v \cdot N^{\text{sat}}}{\rho \cdot E_{\text{P,ISO}}} \tag{16}$$

where D_v is the diffusion coefficient for water vapor in air (2.65×10^{-5} m^2 s^{-1}), ρ is the density of water (1000 kg m^{-3}), N^{sat} is the density of saturated water vapor. R_{eff} is the isotope ratio at z = 0. n is the porosity of the soil.

[33] The decay length λ results from the fit of the exponential curve to the data. It is given by

$$\lambda = z_v + z_l = \frac{1}{E_{\text{P,ISO}}} \left(\theta \cdot f \cdot D + f \cdot D_v (n - \theta) \frac{N^{\text{sat}}}{\rho} \right) \tag{17}$$

After fitting λ, equation (17) can be solved for $E_{\text{P,ISO}}$.

4.2.2. Soil Sampling and Extraction of Soil Water

[34] Soil samples were collected during a field campaign. Any kind of evaporative loss will change the isotopic signature. All soil samples therefore were sealed in containers and weighed. A change of weight can only be related to evaporation. Of the 64 samples taken on nonirrigated sites, 58 had a weight loss below 0.5%. The 6 remaining samples had a significant loss of water and no longer represented the isotopic signature of the field conditions. The stationwise average of the water content varied between 11% and 30%. The locations of the sampling stations are presented in Figure 7.

[35] Even though soil samples were taken at stations in the Yanqi basin with a depth to groundwater as small as 0.5 m, the station with the smallest depth to groundwater used to calculate phreatic evaporation was 0.7 m. It is very difficult to obtain a sufficient amount of soil samples at locations with a depth to groundwater smaller than 0.7 m. The vertical resolution of the samples was 0.1 m. Below that depth, special equipment is required to take soil samples with a vertical height smaller than 0.1 m.

[36] A method described by *Revesz and Woods* [1990] allows extracting soil water from the samples without changing the isotopic signature. Water and toluene form an azeotropic mixture: The toluene-water mixture has a boiling point of 84.1°C, significantly below the boiling point of its constituents (100°C for water, 110°C for toluene). By distilling

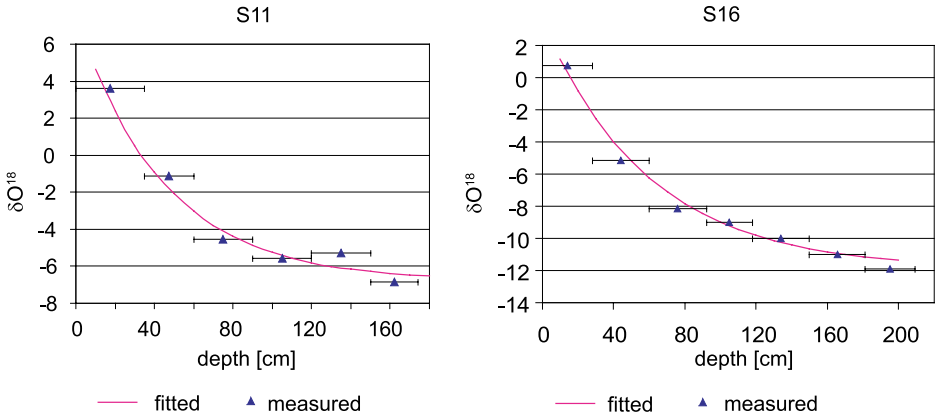

Figure 8. Two examples of $\delta^{18}O$ profiles obtained in the Yanqi basin.

this azeotropic mixture, the water in the soil can be extracted without leaving traces of water in the soil pores. All 58 samples were prepared according to this method.

[37] The oxygen isotopic composition of the water was determined by equilibration with CO_2 on an automated ISOPREP 18 equilibration device coupled to a FISONS-OPTIMA mass spectrometer. The results are reported in the conventional per mil notation with respect to the Vienna Standard Mean Ocean Water (VSMOW). The analytical reproducibility is 0.01%. $\delta^{18}O$ profiles for two different measurement stations are plotted in Figure 8.

4.2.3. Interpretation of Isotopic Profiles

[38] The evaporation rate of 7 stations was calculated by fitting the decay length of the exponential function (section 4.2.1). Diffusion coefficients and the water content were assumed constant for every station. The water content and porosity used represent the average values of the soil profile. The tortuosity was assumed constant for all stations. These are crude assumptions and they limit the reliability of the absolute value estimated. The influence of these assumptions is discussed in the final chapter of this paper.

5. Results

5.1. Interpretation of the Stable Isotope Profiles

[39] Apart from the comparison with the remote sensing images, the calculated evaporation rates by themselves yield useful information: A relation between the depth to groundwater and the evaporation rate can be established. Figure 9 plots the results of the analysis in the Yanqi basin as well as results presented by *Hu et al.* [2003]. Hu established a relation between phreatic evaporation and depth to groundwater for a different type of soil, located close to the Tarim river in Aksu, about 450 km to the west of the Yanqi basin. The shape of these relations is in agreement with *Coudrain-Ribstein et al.* [1998], who concluded that, regardless of the soil type, the relation between the depth to groundwater and phreatic evaporation is concave. The relation between depth to groundwater and phreatic evaporation is of great importance for the basin's water balance. If quantified, such a relation can be included in a groundwater model to calculate phreatic evaporation. This function was estimated for the Yanqi basin and is plotted in Figure 9.

[40] *Hu et al.* [2003] reported a significant increase of phreatic evaporation up to the potential evaporation (for Aksu) of 1.2 m a^{-1}, if the groundwater was closer than 0.53 m to the surface. This depth to groundwater is called d_{ext1}. In our approach, it was assumed that d_{ext1} is the same as observed by Hu et al. By extrapolating the linear relationship, the extinction depth d_{ext2} for the Yanqi basin is around 2.7 m. It was obtained by extrapolating the relation between $E_{P,ISO}$ and the depth to groundwater to an evaporation rate of zero.

5.2. Extracting Phreatic Evaporation From NOAA-ET

[41] On the basis of the estimates of $ET_{V,NOAA}$ at all measurement stations and the map of the NDVI, a relation between the two quantities can be established. In Figure 10, $ET_{V,NOAA}$ and ET_{NOAA} are plotted vs. the average NDVI (year 2000). The comparison was carried out on a 2 km by 2 km scale. The lower resolution was obtained by averaging. Minimum and maximum values of the pixels included in a 2 km by 2 km pixel are plotted as error bars.

[42] The linear regression analysis between $ET_{V,NOAA}$ and the NDVI yields

$$ET_{V,NOAA} = 4381 \cdot NDVI - 29.5,\ R^2 = 0.888 \qquad (18)$$

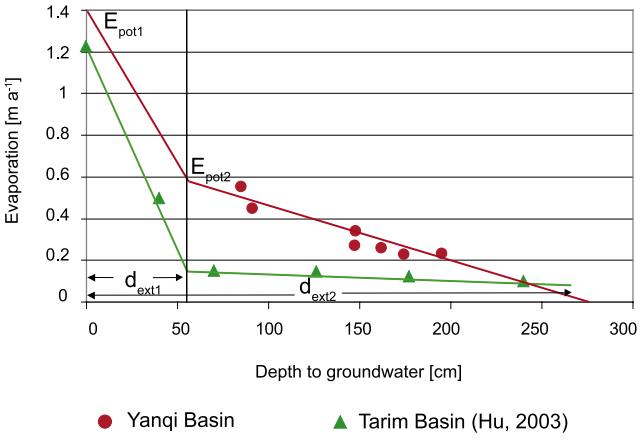

Figure 9. Phreatic water evaporation versus depth to groundwater. E_{pot1} equals the potential evapotranspiration rate of Yanqi basin (1.4 m a^{-1}). The linear fit through the phreatic evaporation is used between the extinction depth and d_{ext1}. The evaporation rate at d_{ext1} is called E_{pot2}.

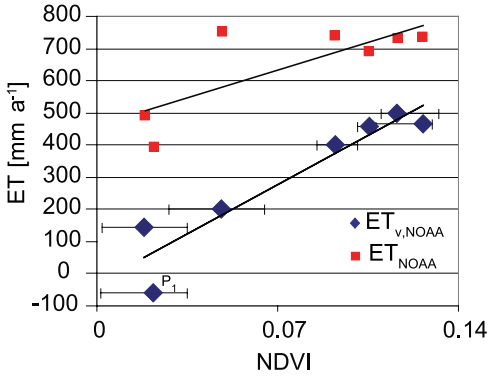

Figure 10. $ET_{V,NOAA}$ and ET_{NOAA} versus the annual average of the NDVI (for the pixels the isotope sampling site are located). $ET_{V,NOAA}$ was calculated with equation (4). Phreatic evaporation accounts for the difference between $ET_{V,NOAA}$ and ET_{NOAA}. The point P1 is less than zero and is discussed in section 6.4.

The regression of $ET_{V,NOAA}$ on NDVI is highly significant ($P < 0.0015$). R^2 between the total ET rate (ET_{NOAA}) and the NDVI is only 0.6, significantly smaller than the one between $ET_{V,NOAA}$ and the NDVI. Phreatic evaporation accounts for up to 60% of evapotranspiration at the stations plotted.

[43] The reason why the comparison was carried out on a 2 km by 2 km basis is the uncertainty of the georeference. The locations of the sampling stations were determined by using a hand-held GPS with an accuracy of around 10 m. However, the accuracy of the georeference of the NOAA-AVHRR images is in the range of one pixel. The uncertainty of the georeference made it impossible to compare the measurements on a 1 km by 1 km resolution, as four measurement stations are located so close to the border of a pixel that a comparison on a 1 km by 1 km basis may be misleading.

5.3. Map of Phreatic Evaporation

[44] The upper half of Figure 11 shows a map of phreatic evaporation. It was generated by subtracting $ET_{V,NOAA}$ from the annual ET_{NOAA}. $ET_{V,NOAA}$ was calculated using the map of NDVI and the relation found in (18). Figure 11 indicates that the highest evaporation rates found are in the close vicinity of the little lake and along the rivers. These areas all exhibit a small depth to groundwater. The irrigated areas also feature an increased phreatic evaporation rate. Within the irrigated area, phreatic evaporation accounts for 36% of the total annual ET.

[45] *Brunner et al.* [2007] presented a method to map soil salinity of the topsoil with remotely sensed data. The salt map was calculated by regionalizing measurements of soil electrical conductivity with spectral similarity maps. The spectral similarity maps were calculated with spectral correlation mapping techniques using image-based reference spectra of saline areas. The comparison of a salt map calculated for the Yanqi basin and the map of phreatic evaporation is instructive. The soil salinity map represents a long-term integral over time of the phreatic evaporation. The phreatic evaporation rates in Figure 11, however, were calculated considering only data of 1 year. The two quantities are therefore only expected to match in areas where the depth to groundwater has been very shallow for a long time. The areas around Bostan Lake have always had a very small depth to groundwater. Not surprisingly, both phreatic evaporation as well as the salinity values are high. If high values of phreatic evaporation are found in areas with low salinity, the groundwater table has only in recent years come close to the surface.

[46] Such areas can easily be identified in Figure 11, and the statement that soil salinity is driven by phreatic evaporation is confirmed. For example, irrigation in the areas north of the Kaidu river at location 1 (see phreatic evaporation in Figure 11) was intensified from the year 1995 to 2000. As a consequence, the groundwater table has been rising and has already reached a critical level, which is above the extinction depth. However, the transport of the salt stored in the aquifer to the soil surface has only been going on for the time the groundwater table has been above the extinction depth. The amount of salt at the soil surface is therefore small compared to the amount of salt that accumulated in the topsoil around the lake. Area 2 in Figure 11 is similar to area 1: Soil salinity will become more and more severe if the high evaporation rates are maintained by ongoing irrigation. The effect of drainage is clearly visible at location 3. Even though this area has been irrigated for a very long time, the extent of soil salinity over the nonirrigated patches does not reach the high levels of soil salinity in the areas south of location 3.

[47] The effect of overirrigation on the distribution of salt is clearly visible around area 4. The very high salinity values in this area are abruptly followed by an area with relatively low soil salinity in the north. In the seventies, attempts were made to use the entire area for crop production. The area was irrigated and it appeared that the salt was flushed down. However, the depth to groundwater was very shallow even before irrigation took place, and the applied irrigation water quickly evaporated. Instead of flushing down the salt, the effect of irrigation was the accumulation of salt close to the surface. The depth to groundwater table slightly north of the area number 4 is increasing rapidly. In this area, overirrigation has, at least for a certain time, the desired effect: flushing the salt stored in the root zone down into the aquifer.

6. Discussion

[48] Both the calculation of remotely sensed ET (ET_{NOAA}), and the determination of $E_{P,ISO}$ contain uncertainties and several assumptions have been made implicitly. These points are discussed in the following sections.

6.1. $\delta^{18}O$ and $E_{P,ISO}$

[49] The accuracy of the measurements as well as the procedure during sampling are considered reliable. Changes of the water content during the storage and the transport of the soil samples were very small. Documenting the weight allowed to control this uncertainty. Even though the measurement of the isotopic data is considered accurate, the resulting estimates of phreatic evaporation contain uncertainties as assumptions had to be made in the interpretation of the stable isotope profile. All coefficients used to calculate the evaporation rate were considered constant. The temperature profile in the soil is unknown and therefore the temperature dependency of the self diffusion coefficient

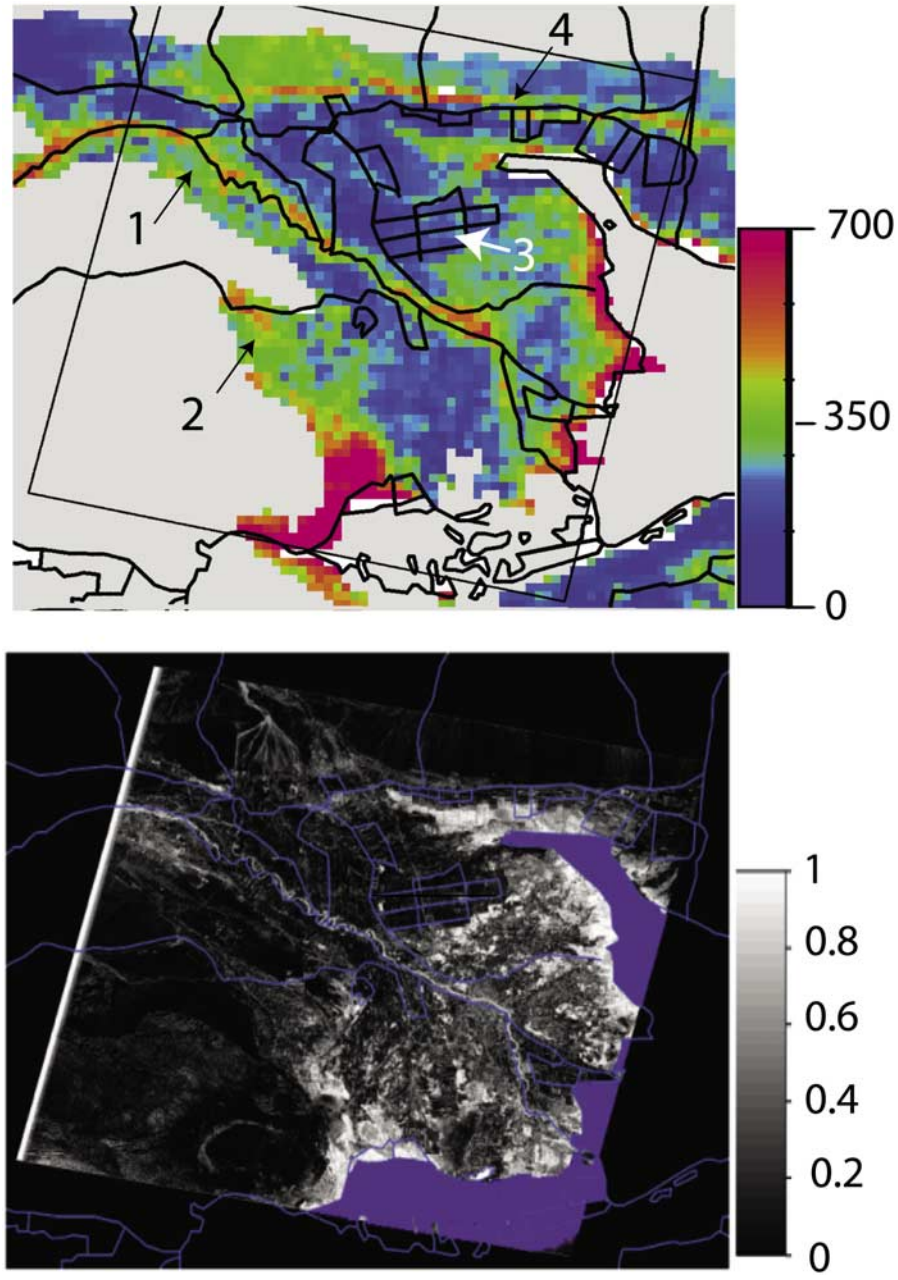

Figure 11. Phreatic evaporation for the year 2000 (mm a^{-1}) and the soil salinity map, presented in units of spectral similarity to a completely salinized pixel. Both maps are overlaid by the drainage system of the basin.

is neglected. Even though *Barnes and Allison* [1988] point out that the temperature effects on the profile are minor, the absolute value of phreatic evaporation is directly proportional to the diffusion coefficient. A possible option reducing this uncertainty would be to measure the temperature of groundwater at the sampling locations, as the temperature of groundwater does, to a certain extent, reflect the average annual surface temperature. However, such data have not been obtained and the diffusion coefficient was determined from the annual average air temperature.

6.2. ET

[50] The absolute value of annual evapotranspiration estimated by using remote sensing is uncertain. Besides the sources of uncertainty pointed out by *Roerink et al.* [2000], the conversion of the channel albedos to a broadband albedo was carried out by using standard parameters described by *Valiente et al.* [1995]; these conversion parameters have not been determined for the Yanqi basin. The parameters required to calculate the surface temperature were not measured in the field. However, the high correlation between the potential ET and ET_{NOAA} as well as the stable ET patterns show that the pattern information is consistent.

6.3. $E_{P,ISO} = E_{P,NOAA}$

[51] It was assumed that $E_{P,ISO}$ equals $E_{P,NOAA}$. This means that the value $E_{P,ISO}$ calculated on the basis of stable

isotopes is representing the phreatic evaporation rate over the entire area of the remote sensing pixel. This assumption implies that the presence of irrigated vegetation does not significantly influence phreatic evaporation. In case of limiting energy and a dense vegetation cover, this influence can be significant. However, in the Yanqi basin evapotranspiration is not energy limited and the vegetation cover is not dense. The average ET over the irrigated area is 650 mm/a (see Figure 6). This is far below the potential evaporation rate. This confirms that water and not energy is limiting evapotranspiration. Despite the excess of energy, a dense vegetation cover would have an influence on the phreatic evaporation rate. We assume that this influence is not significant because of the relatively low vegetation density. Even within the intensely irrigated areas in the center of the basin, the network of fields is patchy and the crops are not planted densely.

6.4. Absolute Values and Relative Uncertainty

[52] We pointed out that the absolute values of both ET_{NOAA} and $E_{P,ISO}$ are uncertain. An overestimation of $E_{P,NOAA}$ compared to $E_{P,ISO}$ results in an overestimation of the final phreatic evaporation map and vice versa. Nevertheless, even if there is a bias in the absolute values, the pattern information of phreatic evaporation still remains consistent. One indication that there is a shift between the absolute values is point P1 in Figure 10: the difference between ET_{NOAA} and $E_{P,ISO}$ is negative. This can be related to a systematic bias in ET_{NOAA}, $E_{P,ISO}$ or both.

6.5. $ET_{V,NOAA}$

[53] In this approach, the transpiration rates of the irrigated areas and excess irrigation water were lumped into one parameter. This implies that the irrigation efficiency as well as the dependency of the NDVI on the amount of water available is constant. This assumption limits the method to relatively coarse resolutions. On the field scale this relation may not hold if for example two different crops are planted next to each other or if the irrigation efficiency varies significantly over a short scale. However, the relatively coarse spatial resolution of the NOAA satellite leads to an averaging of the these effects. Given the fact that there is no large-scale variation of the crop mix as well as the efficiency of the irrigation within the basin, no systematic bias between the different irrigation districts is expected.

7. Conclusions

[54] Simple remote sensing methodologies are employed to retrieve ET estimates requiring minimal ancillary data. While the methods have significant uncertainty, the spatial patterns in the resulting map of phreatic evaporation are reasonable and useful for identifying general areas of high risk to salinization. A string of assumptions has been made and it is extremely difficult if not impossible to assess the influence of every assumption or simplification accurately. Nevertheless, a very good correlation between the NDVI and $ET_{V,NOAA}$ could be established. Even though the correlation coefficient is high, the absolute quantities remain uncertain. A correlation between $ET_{V,NOAA}$ rates and the NDVI can also be found if the absolute quantities are systematically biased. This method does not claim to yield accurate absolute values; the uncertainties are too large. Nevertheless, the pattern of phreatic evaporation can be extracted from the distribution of evapotranspiration. The goal of the study of identifying regions endangered by soil salinization, can be achieved on the basis of this pattern information. Furthermore, spatial patterns contain information that can be used in groundwater modeling, even if the absolute values are uncertain. For example, *Hendricks Franssen et al.* [2008] showed how uncertain pattern information could improve the model calibration.

[55] The fact that this method can separate the two quantities in the Yanqi basin is reflected in the significantly higher correlation coefficient between the NDVI and $ET_{V,NOAA}$ compared to the correlation coefficient between the NDVI and ET_{NOAA}. The qualitative comparison of the salt map with the distribution of phreatic evaporation confirms that the pattern information obtained is valid.

[56] The method can be applied to other project areas with similar climatic conditions provided that irrigated and nonirrigated sites are present. If rainfall is significant, the quantification of phreatic evaporation on the basis of stable isotopes is not possible. However, other methods to estimate the phreatic evaporation rate are available.

[57] **Acknowledgments.** We are grateful for the help of Stephano Bernasconi; without his support in analyzing the soil water this study would not have been possible. We are also grateful to Daniel Braun and his laboratory staff, who provided support in extracting the soil water. Many thanks also go to Jemet Krambula, our driver in the Yanqi basin. His knowledge of the project area significantly contributed to this study. Financial support for this project has been granted by the Department of Civil, Environmental and Geomatic Engineering, ETH Zurich. We do also want to thank the three anonymous reviewers. Their comments helped to significantly improve this manuscript.

References

Allen, R., L. Pereira, D. Raes, and M. Smith (1998), Crop evapotranspiration—Guidelines for computing crop water requirements, *Irrig. Drain. Pap. 56*, Food and Agric. Organ. of the U. N., Rome.

Allen, R. G., M. Tasumi, and R. Trezza (2007), Satellite-based energy balance for mapping evapotranspiration with internalized calibration (metric)—Model, *J. Irrig. Drain. Eng.*, *133*(4), 380–394.

Barnes, C. J., and G. B. Allison (1988), Tracing of water-movement in the unsaturated zone using stable isotopes of hydrogen and oxygen, *J. Hydrol.*, *100*(1–3), 143–176.

Bastiaanssen, W., M. Menenti, R. Feddes, and A. Holtslag (1998a), A remote sensing surface energy balance algorithm for land (SEBAL)—1. Formulation, *J. Hydrol.*, *213*(1–4), 198–212.

Bastiaanssen, W. G. M., H. Pelgrum, J. Wang, Y. Ma, J. F. Moreno, G. J. Roerink, and T. van der Wal (1998b), A remote sensing surface energy balance algorithm for land (SEBAL)—2. Validation, *J. Hydrol.*, *213*(1–4), 213–229.

Brunner, P., H. T. Li, W. Kinzelbach, and W. P. Li (2007), Generating soil electrical conductivity maps at regional level by integrating measurements on the ground and remote sensing data, *Int. J. Remote Sens.*, *28*(15), 3341–3361.

Brutsaert, W., and M. Sugita (1992), Application of self-preservation in the diurnal evolution of the surface-energy budget to determine daily evaporation, *J. Geophys. Res.*, *97*(D17), 18,377–18,382.

Carlson, T. N., and M. J. Buffum (1989), On estimating total daily evapotranspiration from remote surface-temperature measurements, *Remote Sens. Environ.*, *29*(2), 197–207.

Carlson, T. N., W. J. Capehart, and R. R. Gillies (1995), A new look at the simplified method for remote-sensing of daily evapotranspiration, *Remote Sens. Environ.*, *54*(2), 161–167.

Chen, T. S., and G. Ohring (1984), On the relationship between clear-sky planetary and surface albedos, *J. Atmos. Sci.*, *41*(1), 156–158.

Coll, C., and V. Caselles (1997), A split-window algorithm for land surface temperature from advanced very high resolution radiometer data: Validation and algorithm comparison, *J. Geophys. Res.*, *102*(D14), 16,697–16,713.

Coudrain-Ribstein, A., B. Praxt, A. Talbi, and C. Jusserand (1998), Is evaporation from phreatic aquifers in arid zones independent of the soil characteristics?, *C. R. Acad. Sci., Ser. IIa Sci. Terre Planetes*, *326*(3), 159–165.

Courault, D., B. Seguin, and A. Olioso (2005), Review on estimation of evapotranspiration from remote sensing data, *Irrig. Drain. Syst.*, *19*(3–4), 223–249.

Crago, R. D. (1996), Conservation and variability of the evaporative fraction during the daytime, *J. Hydrol.*, *180*(1–4), 173–194.

Craig, H., and L. Gordon (1965), Deuterium and oxygen-18 variations in the ocean and marine atmosphere, in *Stable Isotopes in Oceanographic Studies and Paleo-Temperatures*, edited by E. Tongiorgi, pp. 9–130, Cons. Naz. delle Ric., Pisa, Italy.

Dong, X., T. Jiang, and H. Jiang (2001), Study on the pattern of water resources utilisation and environmental conservation of Yanqi basin, in *Development, Planning and Management of Surface and Groundwater Resources*, *IHR Congr. Proc.*, vol. A, edited by G. Li, pp. 333–340, Tsinghua Univ. Press, Beijing.

French, A. N., T. J. Schmugge, W. P. Kustas, K. L. Brubaker, and J. Prueger (2003), Surface energy fluxes over El Reno, Oklahoma, using high-resolution remotely sensed data, *Water Resour. Res.*, *39*(6), 1164, doi:10.1029/2002WR001734.

Gurney, R., and A. Hsu (1990), Relating evaporative fraction to remotely sensed data at the FIFE site, paper presented at Symposium on FIFE, Am. Meteorol. Soc., Anaheim, Calif.

Hendricks Franssen, H. J., P. Brunner, P. Makobo, and W. Kinzelbach (2008), Equally likely inverse solutions to a groundwater flow problem including pattern information from remote sensing images, *Water Resour. Res.*, *44*, W01419, doi:10.1029/2007WR006097.

Hillel, D. (2000), *Salinity Management for Sustainable Irrigation: Integrating Science, Environment and Economics*, World Bank, Washington, D. C.

Hu, S., S. Kang, Y. Song, and X. Ceng (2003), Calculating phreatic water evaporation from bare soil for the Tarim River basin, Xinjiang, in *International Conference on Water-Saving Agriculture and Sustainable Use of Water and Land Resources in Arid and Semiarid Areas*, edited by S. Kang et al., pp. 727–733, Shaanxi Sci. and Technol. Press, Yanglin, China.

Jakeman, A. J., H. A. Nix, and F. Ghassemi (1995), *Salinisation of Land and Water Resources: Human Causes, Extent and Management*, CAB Int., Wallingford, U. K.

Jiang, L., and S. Islam (1999), A methodology for estimation of surface evapotranspiration over large areas using remote sensing observations, *Geophys. Res. Lett.*, *26*(17), 2773–2776.

Jiang, L., and S. Islam (2001), Estimation of surface evaporation map over southern Great Plains using remote sensing data, *Water Resour. Res.*, *37*(2), 329–340.

Kempf, S. K., and S. W. Tyler (2006), Spatial characterization of land surface energy fluxes and uncertainty estimation at the Salar de Atacama, northern Chile, *Adv. Water Resour.*, *29*(2), 336–354.

Kustas, W. P., and J. M. Norman (1996), Use of remote sensing for evapotranspiration monitoring over land surfaces, *Hydrol. Sci. J.*, *41*(4), 495–516.

Kustas, W. P., E. M. Perry, P. C. Doraiswamy, and M. S. Moran (1994), Using satellite remote-sensing to extrapolate evapotranspiration estimates in time and space over a semiarid rangeland basin, *Remote Sens. Environ.*, *49*(3), 275–286.

Laymon, C., D. Quattrochi, E. Malek, L. Hipps, J. Boettinger, and G. McCurdy (1998), Remotely-sensed regional-scale evapotranspiration of a semi-arid great basin desert and its relationship to geomorphology, soils, and vegetation, *Geomorphology*, *21*(3–4), 329–349.

Lin, A., B. Fu, K. Kano, T. Maruyama, and J. Guo (2002), Late quaternary right-lateral displacement along active faults in the Yanqi basin, southeastern Tian Shan, northwest China, *Tectonophysics*, *354*(3–4), 157–178.

Menenti, M., and B. Choudhury (1993), Parametrization of land surface evapotranspiration using a location dependent potential evapotranspiration and surface temperature range, in *Exchange Processes at the Land Surface for a Range of Space and Time Scales*, edited by H. Bolle, *IAHS Publ.*, *212*, 561–568.

Mills, R. (1973), Self-diffusion in normal and heavy-water in range 1–45 degrees, *J. Phys. Chem.*, *77*(5), 685–688.

Nagler, P. L., J. Cleverly, E. Glenn, D. Lampkin, A. Huete, and Z. M. Wan (2005), Predicting riparian evapotranspiration from MODIS vegetation indices and meteorological data, *Remote Sens. Environ.*, *94*(1), 17–30.

Nishida, K., R. R. Nemani, S. W. Running, and J. M. Glassy (2003), An operational remote sensing algorithm of land surface evaporation, *J. Geophys. Res.*, *108*(D9), 4270, doi:10.1029/2002JD002062.

Parodi, G. (2002), AHAS algorithms and theory. AHVRR hydrological analysis system: Algorithms and theory, version 1.3, Int. Inst. for Geo Inf. Sci. and Earth Obs., 77 pp., Enschede, Netherlands.

Revesz, K., and P. H. Woods (1990), A method to extract soil-water for stable isotope analysis, *J. Hydrol.*, *115*(1–4), 397–406.

Richards, L. (1954), Diagnosis and improvement of saline and alkali soils, *Agric. Handb. 60*, U.S. Dep. of Agric., Washington, D. C.

Rodriguez, E., C. Morris, J. Belz, E. Chapin, J. Martin, W. Daffer, and S. Hensley (2005), An assessment of the SRTM topographic products, *Tech. Rep. JPL D-31639*, Jet Propul. Lab., Pasadena, Calif.

Roerink, G. J., Z. Su, and M. Menenti (2000), S-SEBI: A simple remote sensing algorithm to estimate the surface energy balance, *Phys. Chem. Earth, Part B*, *25*(2), 147–157.

Shuttleworth, W., R. Gurney, A. Hsu, and J. Ormsby (1989), FIFE: The variation in energy partition at surface flux sites, in *Remote Sensing and Large-Scale Global Processes*, edited by A. Rango, *IAHS Publ.*, *186*, 67–74.

Su, Z. (2002), The surface energy balance system (SEBS) for estimation of turbulent heat fluxes, *Hydrol. Earth Syst. Sci.*, *6*(1), 85–99.

Sugita, M., and W. Brutsaert (1991), Daily evaporation over a region from lower boundary-layer profiles measured with radiosondes, *Water Resour. Res.*, *27*(5), 747–752.

Thunnissen, H. A. M., and G. J. A. Nieuwenhuis (1990), A simplified method to estimate regional 24-h evapotranspiration from thermal infrared data, *Remote Sens. Environ.*, *31*(3), 211–225.

Tyler, S. W., S. Kranz, M. B. Parlange, J. Albertson, G. G. Katul, G. F. Cochran, B. A. Lyles, and G. Holder (1997), Estimation of groundwater evaporation and salt flux from Owens Lake, California, USA, *J. Hydrol.*, *200*(1–4), 110–135.

Ullman, W. J. (1995), The fate and accumulation of bromide during playa salt deposition—An example from Lake Frome, South Australia, *Geochim. Cosmochim. Acta*, *59*(11), 2175–2186.

Valiente, J. A., M. Nunez, E. Lopezbaeza, and J. F. Moreno (1995), Narrow-band to broad-band conversion for Meteosat-visible channel and broad-band albedo using both AVHRR-1 and AVHRR-2 channels, *Int. J. Remote Sens.*, *16*(6), 1147–1166.

Wallace, J. M., and P. V. Hobbs (2006), *Atmospheric Science: An Introductory Survey*, *Int. Geophys. Ser.*, vol. 92, 2nd ed., Academic, Oxford, U. K.

Zhang, L., and R. Lemeur (1995), Evaluation of daily evapotranspiration estimates from instantaneous measurements, *Agric. For. Meteorol.*, *74*, 139–154, doi:10.1016/0168-1923(94)02181-I.

Zimmermann, U., D. Ehalt, and K. Münnich (1967), Soil water movement and evapotranspiration: Changes in the isotope composition of water, in *Isotopes in Hydrology*, pp. 567–584, Int. At. Energy Agency, Vienna.

P. Brunner, School of Chemistry, Physics and Earth Sciences, Flinders University, GPO Box 2100, Adelaide, SA 5001, Australia. (philip.brunner@flinders.edu.au)

X. G. Dong, Xinjiang Agricultural University, Urumqi, China.

W. Kinzelbach and H. T. Li, Institute of Environmental Engineering, ETH Zurich, CH-8093 Zurich, Switzerland.

W. P. Li, China Institute of Geo-Environmental Monitoring, Number 20 Dahuisi, Haidian District, Beijing, 100081, China.